FINAL REPORT TO

PACIFIC EARTHQUAKE ENGINEERING RESEARCH CENTER

LIFELINES PROGRAM TASK 1A03

3D GROUND MOTION SIMULATION IN BASINS

Period of Performance: August 1, 2002 – March 31, 2004

Coordinating P. I.: Steven M. Day, San Diego State University
Co-Investigators: Jacobo Bielak, Carnegie-Mellon University
                   Doug Dreger, University of California, Berkeley
                   Shawn Larsen, Lawrence Livermore National Laboratory
                   Robert Graves & Arben Pitarka, URS Corporation
                   Kim B. Olsen, San Diego State University

JUNE 9, 2005

SUMMARY

We simulate long-period (0-0.5 Hz) ground motion time histories for a suite of sixty scenario earthquakes (Mw 6.3 to Mw 7.1) within the Los Angeles basin region. Fault geometries are based upon the Southern California (SCEC) Community Fault Model, and 3D seismic velocity structure is based upon the SCEC Community Velocity Model. The ground motion simulations are done using 5 different 3D finite difference and finite element codes, and we perform numerous cross-check calculations to ensure consistency among these codes. The nearly 300,000 synthetic time histories from the scenario simulations provide a resource for ground motion estimation and engineering studies of large, long-period structures, or smaller structures undergoing large, nonlinear deformations.

By normalizing spectral accelerations to those from simulations performed for reference hard-rock models, we characterize the source-averaged effect of basin depth on spectral acceleration. For this purpose, we use depth (D) to the 1.5 km/s S velocity isosurface as the predictor variable. The resulting mean basin-depth effect is period dependent, and both smoother (as a function of period and depth) and higher in amplitude than predictions from local 1D models. For example, relative to a reference hard-rock site, sites with D equal to 2.5 km (corresponding to some of the deeper L.A. basin locations) have a predicted mean amplification factor of approximately 5.5 at 2 s period, and approximately 7.5 at 10 s period.

The basin amplification estimates described in this report are intended to guide the design of functional forms for use in attenuation relationships for elastic response spectra. In particular, they should be useful guides for extrapolating the period-dependence of basin terms to periods longer than a few seconds, where empirical data provide little constraint. More direct, quantitative use of the results may become possible in the future, however. The main requirement is that we first carefully assess the extent to which the basin effect, as defined and quantified in this study, is already accounted for implicitly in existing attenuation relationships, through (1) departures of the average "rock" site from our idealized reference model, and (2) correlation of basin depth with other predictor variables (such as Vs_{30}). We compare long-period (5 s) spectral amplitudes from the reference simulations with standard regression relationships for sites nominally classified as "rock" in empirical studies. From that comparison, we infer that the average nominal rock site represented in the empirical regression models has response approximately a factor of 2 higher than our hard-rock reference model. Hence, the basin-depth factors can be scaled down by a factor of approximately 2, as a first step toward interpreting them as basin corrections to empirical rock-site relationships.

The factor of 2 long-period bias between hard-rock simulations and empirical rock-site regression models suggests that the standard rock-site classification actually incorporates sites in which relatively low S velocities (less than ~2 km/s) extend, on average, to depths of the order of 0.5 km. Our preliminary recommendation, therefore, is that the basin response functions be used as a guide to the functional form of the depth

and period dependence of the basin effect for depths (to the 1.5 km/s isosurface) greater than about 400-500 m.

INTRODUCTION

The principal aim of this project is to apply 3D numerical modeling to improve understanding of the effects of sedimentary basins on long-period (≥ ~2 seconds) earthquake ground motion. The study employs both finite element and finite difference methods to compute ground motion from propagating earthquake sources in the Southern California Earthquake Center (SCEC) Community Velocity Model (CVM), a 3D seismic velocity model for southern California. This is a joint project between PEER and SCEC, for which matching support was provided by SCEC, with additional support through the SCEC Community Modeling Environment (CME) collaboration.

Previous work under PEER Lifelines projects 1A01 and 1A02 (with SCEC matching support) documented the mathematical soundness of the 5 simulation codes used for the project. Code verification was carried out by exercising the codes on a systematic, collaboratively-defined set of test simulations. In the first stage of these tests (1A01), the codes were validated for simple sources and geometries (Day et al, 2001). The second stage (1A02) tested the codes for point sources and finite, propagating sources in the SCEC CVM, a model that we believe captures many of the complexities present in the earth (Magistrale et al., 2000). Comparisons show that all 5 codes are accurate for these classes of problems (Day, 2003). These tests also demonstrated the validity of putting a lower threshold on the velocity model to exclude S wave velocity values in the CVM that fall below 500 m/s. The tests confirmed that imposing this threshold (for the sake of computational efficiency) had negligible effects within the target bandwidth of 0-0.5 Hz.

For the current investigation, we compute long-period ground motion in the SCEC CVM for a suite of 60 earthquake scenarios. The 3-component ground motion time histories from these scenarios are saved on a grid of 1600 sites covering the Los Angeles region, including sites in the Los Angeles, San Fernando, and San Gabriel basins, as well as rock sites in the intervening areas.

The results from the current study take 2 forms: (1) We have saved and archived a library of time histories from the 60 scenarios. In cooperation with the SCEC CME project, these time histories are available online, through a web interface specialized to engineering applications. These long-period time histories capture basin amplifications, rupture-propagation-induced directivity, and 3D seismic focusing phenomena. They are suitable for the engineering analyses of large, long-period structures, and smaller structures undergoing large, nonlinear deformations. (2) The results of the simulation suite have been analyzed to estimate response spectral amplification effects as a function of basin depth and period. The resulting mean response has been characterized parametrically and provided to the Next Generation Attenuation (NGA) project to guide development of attenuation relations in the empirical (NGA-E) phase of the project.

CODES

Five different codes are employed. These five codes are denoted by four-character abbreviations indicating the respective institutions: UCSB, UCBL, WCC1 (Robert Graves's URS code), WCC2 (Arben Pitarka's URS code), and CMUN. Of these, four are finite difference (FD), and one is finite element (FE).

All of the FD codes (UCSB, UCBL, WCC1, and WCC2) use uniform, structured grids, with staggered locations of the velocity and stress components and fourth-order accurate spatial differencing of the elastodynamic equations. The codes were independently programmed. The main variations among them include: degree of computational parallelism, type of memory management (e.g., main-memory contained operation versus roll-in/roll-out from disk), free-surface boundary condition formulation, absorbing boundary formulation, material interface representation (e.g., type of averaging of material properties in vicinity of properties gradients or interface), and source formulation.

The FE code (**CMUN**) uses unstructured gridding, with linear interpolation on tetrahedral elements. Grid generation is done serially (and is often the most time consuming part of a simulation), while equation solving is done in parallel execution, via an automated domain decomposition scheme.

EARTHQUAKE SCENARIOS

This section gives detailed specifications for the 60 earthquake scenarios for which we perform ground motion simulations. We model sources on ten different faults, or fault configurations (for example, the Puente Hills fault is modeled in 3 different segmentation configurations). For each fault, we simulate 6 sources, using combinations of 3 different static slip distributions and 2 hypocenter locations. These are kinematic simulations: rupture velocity, static slip, and the form of the slip velocity function are all specified *a priori*. The 60 simulations were distributed among the investigators, with 10 of the cases (1 for each fault) run by 2 different investigators using their respective (different) codes. These "cross-check" simulations provide a further check on code consistency, and also ensure that we detect any major errors in problem setup.

Model Region

The areal coverage for the 3D models is the 100 km x 100 km region outlined by the green box in Figure 1. The corners of this region are given by the following geographical coordinates:

$$c1 = 118.70000; 33.58000$$
$$c2 = 118.70000; 34.47746$$
$$c3 = 117.61823; 34.47746$$
$$c4 = 117.61823; 33.58000$$

The origin of this model region is at the lower left (southwest) corner:

Lon = 118.7000, Lat = 33.5800

In all simulations, the boundaries of the computational domain (i.e. absorbing boundaries) lie at or outside of this area and extend to a depth of at least 30 km. For the uniform grid FD modelers, a grid spacing of 200 m was used . The finite element grid uses a variable element size, with near-surface elements as small as 30 in dimension.
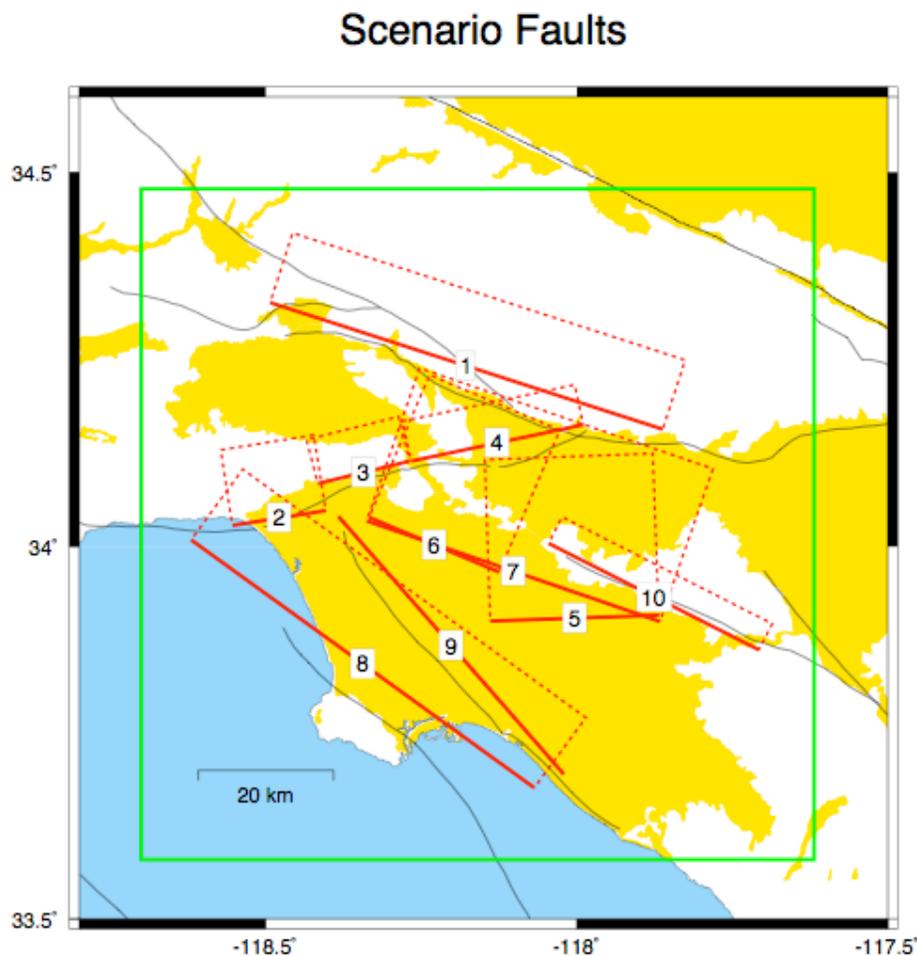
Scenario Faults

Figure 1: Map of scenario events and model region. See Table 1 for fault names and event magnitudes.

Faults

We use the 10 faults listed in Table 1 for the scenario calculations. The surface projections of these faults are also shown in Figure 1. The longitude and latitude coordinates in this table refer to the geographic location of the top center of the fault, that is, the point on the surface that is directly above the midpoint of the top edge of the fault. Strike, dip and rake follows Aki and Richards' convention. Length, width and depth are all given in km. The depth refers to the depth below the surface of the top edge of the fault (0 corresponding to a surface-rupturing event).

TABLE 1: Scenario Faults.

Fault	Lon (TC)	Lat (TC)	M_w	Length	Width	Strike	Dip	Rake	Depth
1) smad	-118.1776	34.2415	7.0	61	18	288	53	90	0
2) smon1	-118.4785	34.0385	6.3	14	14	261	36	45	1
3) hwood	-118.3427	34.0993	6.4	14	19	256	69	70	0
4) raym2	-118.1281	34.1388	6.6	26	17	258	69	70	0
5) ph2e	-118.0037	33.9042	6.8	25	27	268	27	90	3
6) phla	-118.2293	34.0026	6.7	21	26	293	28	90	3
7) phall	-118.1020	33.9670	7.1	46	27	289	27	90	2
8) comp	-118.3440	33.8428	6.9	63	14	306	22	90	5
9) nin	-118.2020	33.8676	6.9	51	16	319	90	180	0
10) whitn	-117.8762	33.9330	6.7	35	15	297	73	160	0

Slip Distributions

For each of the fault geometries, we generate 3 random slip distributions, as realizations of a stochastic model, for use in the simulations. The slip distributions are generated following some empirical rules for the size and distribution of asperities as given by Somerville et al. (1999). The slip values on the fault are drawn from a uniformly distributed random variable, then spatially filtered to give a spectral decay inversely proportional to wavenumber squared, with a corner wavenumber at approximately $1/L$, where L is fault length. Finally, the slip values are scaled to the target moment of the scenario. A representative example is shown in Fig 2.
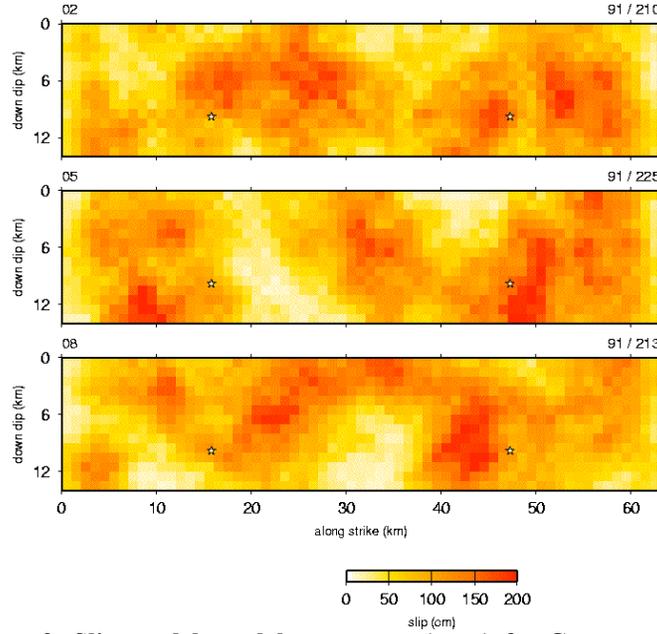
Figure 2. Slip models and hypocenters (stars) for Compton fault scenarios.

Hypocenter Locations

The two hypocenter locations are defined as follows for each fault: Hypocenter 1 is located at an along-strike (AS_1) distance of 0.25 of the fault length and at a down-dip (DD_1) distance of 0.7 of the fault width (measured within the fault plane from the top edge of the fault, not the ground surface). Hypocenter 2 is located at an along strike (AS_2) distance of 0.75 of the fault length and at a down-dip (DD_2) distance of 0.7 of the fault width. Table 2 lists the hypocenter locations (in km) for each of the specific faults. In addition, the two hypocenter locations for a representative case are shown in Fig 2.

Slip Velocity Function

The slip velocity function for each simulation is an isosceles triangle with a base of duration T_r. The value of T_r is magnitude dependent and given by the empirically derived expression (Somerville et al., 1999):

$$\log_{10}(T_r) = 0.5 * (M_w + 10.7) + \log_{10}(2.0 \times 10^{-9})$$

where $\log_{10}$ is base 10 logarithm and M_w is moment magnitude. Table 2 lists the values of T_r for each event.

Table 2: Hypocenters and Rise Times.

Fault	M_w	Hypocenter 1		Hypocenter 2		T_r (s)
		AS_1(km)	DD_1(km)	AS_2(km)	DD_2(km)	
1) smad	7.0	15.25	12.6	45.75	12.6	1.4
2) smon1	6.3	3.5	9.8	10.5	9.8	0.63
3) hwood	6.4	3.5	13.3	10.5	13.3	0.71
4) raym2	6.6	6.5	11.9	19.5	11.9	0.89
5) ph2e	6.8	6.25	18.9	18.75	18.9	1.1
6) phla	6.7	5.25	18.2	15.75	18.2	1.0
7) phall	7.1	11.5	18.9	34.5	18.9	1.6
8) comp	6.9	15.75	9.8	47.25	9.8	1.3
9) nin	6.9	12.75	11.2	38.25	11.2	1.3
10) whitn	6.7	8.75	10.5	26.25	10.5	1.0

Material Properties

All simulations use the SCEC CVM, Version 2, except for modifications described below to impose a lower limit on the velocities and add anelastic attenuation. The unmodified model is described in the Magistrale et al., 2000).

The SCEC model is modified as follows: Replace the SCEC model S velocity with the value 500 m/s whenever the SCEC model value falls below 500 m/s. Whenever this minimum S velocity is imposed, the P wave velocity is set equal to 3 times the S velocity (1500 m/s in this case). Density values follow the SCEC model without modification.

The quality factors for P and S waves, respectively, Q_p and Q_s, are set to the preferred Q model of Olsen et al. (2003), as follows:

$Q_s = 0.02 \times V_s$ (in m/s), when $V_s < 1500$ m/s
$Q_s = 0.1 \times V_s$ (in m/s) when $V_s \geq 1500$ m/s
$Q_p = 1.5 * Q_s$

Rupture Velocity

Rupture velocity is constant for all faults and all slip models. This value is set at 2.8 km/s. The rupture starts at the hypocenter and spreads radially outward from this point at the specified velocity.

Duration

The simulated duration for each scenario is 80 seconds.

OUTPUT

The 3-component time histories are saved on a 2 km x 2 km grid covering the inner 80 km x 80 km portion of the model area. No filtering (other than the source time

function) is applied to the output. The result is 1600 sites for each scenario simulation. The locations of these 1600 points are indicated by the red dots in Fig 3. We use a subset of 16 stations from this grid to do cross-checking of the simulations. These stations are indicated by the black triangles in Fig 3.
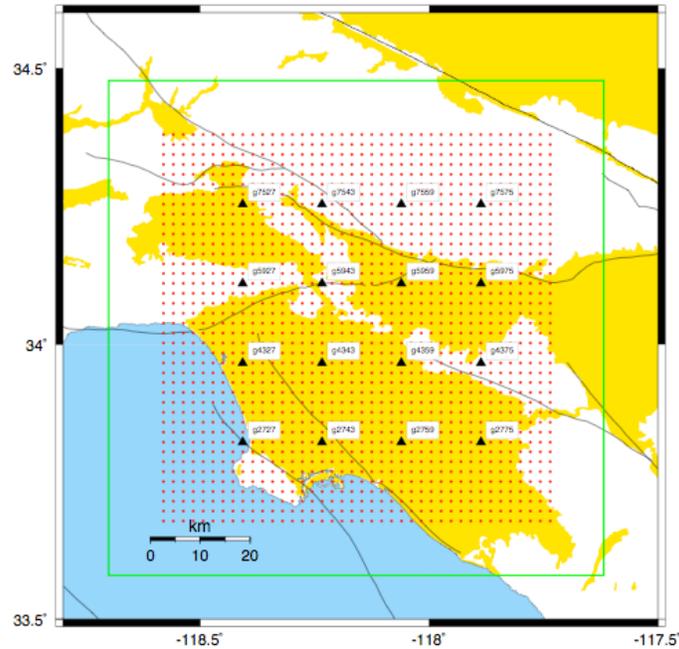
Figure 2. Map of output grid and cross-check stations (triangles)

DIVISION OF LABOR

The distribution of runs was designed to balance the manpower demands in terms of model set-up, while still taking advantage of the CPU power where it is most readily available. Table 3 outlines the distribution of runs among the modeling teams:

Table 3: Distribution of Simulation Runs.

Fault	Modeling Groups				
	UCB-LLNL	UCSB	CMU	URS 1	URS 2
1) smad	f		c		
2) smon1	f		c		
3) hwood	f			c	
4) raym2	f			c	
5) ph2e		f		c	
6) phla		f		c	
7) phall		f			c
8) comp		f			c
9) nin			f		c
10) whitn			f		c

where

f = run full set of 6 realizations for particular fault

9

c = run 1 check realization for particular fault

Each model size is in the range of roughly 10-40 million nodes, with computation time of roughly 300-1000 CPU/hrs per scenario (depending upon code and computer system used).

CROSS-CHECK RESULTS

Figure 4 compares velocity time-history results (north-south component) for one of the scenarios (Sierra Madre fault), as computed by 2 different codes, one finite element (CMUN) and one finite difference (UCBL). Because the finite difference and finite element grids are very different, sampling the SCEC CVM are different points (and with much higher resolution in the near surface in the case of the finite element grid), this comparison is the worst case among the 10 cross-checks that we have. Simulations of the same scenario computed with different finite difference codes produce time histories that are almost indistinguishable.

RESPONSE SPECTRA

For all 60 scenarios, and all sites, we compute response spectral acceleration (Sa), for 5% damping, as a function of period for each component of motion. This is done for 26 periods in the range 2-10 seconds: spectral acceleration is computed at 0.2 second intervals between 2 and 5 second, and at 0.5 second intervals between 5 and 10 seconds. Results files, one for each scenario, are available online. These files contain the following additional information for each of the 1600 output sites: (1) source-receiver distance, according to definitions used in the regression models of Joyner and Boore (1997) and Abrahamson and Silva (1997) definitions, respectively. (2) Sediment depth at the site, as given by 4 measures: depths to 1.0, 1.5, 2.5, and 3.5 km/s S wave velocity isosurfaces.

(URL for spectral files:
    http://www.seismo.berkeley.edu/~dreger/scec-peerbasins.html)
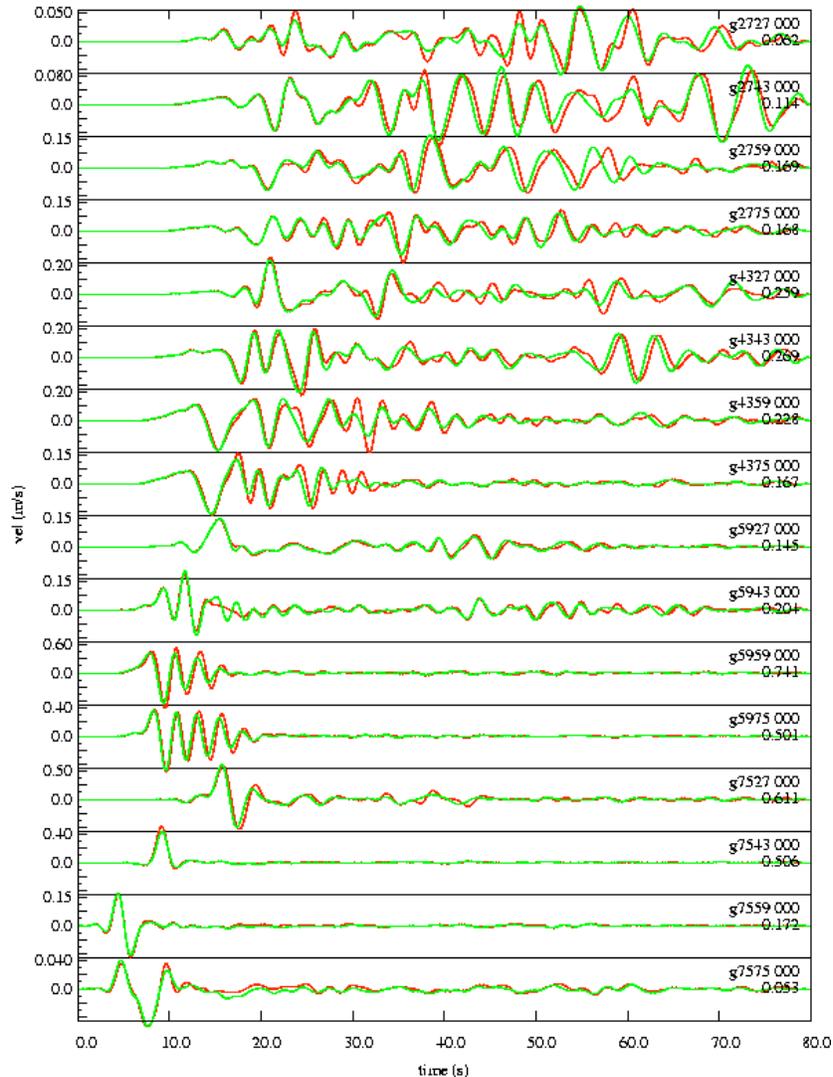
Figure 4. Comparison of finite element (CMUN) and finite difference (UCBL) velocity time histories (N-S component) for one of the Sierra Madre fault scenarios. Results are shown at the 16 sites denoted by triangles in Fig 2.

REFERENCE SIMULATIONS

To aid us in quantifying the effect of sedimentary basins on the computed ground motions, we perform several auxiliary, or "reference," simulations. For each of the 10 faults, we select one rupture scenario, and repeat that simulation using the same source model, but replacing the SCEC CVM with a horizontally stratified model. The stratified model reference model corresponds to an artificially high-velocity, unweathered hard-rock site. This reference velocity model was constructed by laterally extending a vertical profile of the SCEC CVM located at (-118.08333, 34.29167), in the San Gabriel Mountains. As noted, surface S velocities are artificially high (3.2 km/s) in the resulting model, since this part of the SCEC model does not account for a weathered layer. Response spectra for the reference simulations are available from the website cited

11

above. Their purpose is solely to provide a normalization for the results from the simulations done in the full SCEC CMV, as an approximate means of isolating basin effects from source effects.

RESPONSE SPECTRAL AMPLIFICATIONS

Basin amplification effects result from interaction of the wavefield with basin margins, and depend in a complex, poorly understood manner on period, source location, source distance, basin geometry, sediment velocity distribution, and site location within the basin. The 60 scenarios provide synthetic data that can be used to improve our understanding of these effects. We take an initial step in this direction by attempting to isolate the effects of period and local basin depth. To isolate these 2 effects, we average over sources. As response spectral values varies much more between ruptures on different faults than between ruptures on a given fault, we have computed averages using only 1 of the 6 scenarios from each fault, giving us a 10-event subset of the simulations. This subset misses a small amount of the variability in basin response present in the full 60-event suite, but allows us to work with spectral values normalized to the reference structure, without requiring 60 reference-structure simulations. Tests using a small number of additional events confirm that sources effects have been adequately removed by this procedure.

Method

We first bin the sites according to the local basin depth D at a site, with D_j denoting the depth at site j. For this purpose, we define the depth D to be the depth to the 1.5 km/s S wave velocity isosurface. Note, however, in the SCEC CVM, the depths of different S velocity isosurfaces are strongly correlated, and therefore very similar results are obtained using the 1.0 or 2.5 km/s isosurface instead of the 1.5 km/s isosurface. The binning is represented through a matrix W. We define N_{bin} bins by specifying depths D_q^{bin}, q=1, . . . N_{bin}, at the bin centers, spaced at equal intervals ΔD (i.e., $D_q^{bin} = (q-1/2)\Delta D$, and then form W,

$$W_{qj} = \begin{cases} 1 & \text{if} \quad \left(D_q^{bin} - \Delta D/2\right) \leq D_j < \left(D_q^{bin} + \Delta D/2\right) \\ 0 & \text{otherwise} \end{cases}.$$

For consistency with most empirical attenuation relations, we work with response spectral values averaged for the two horizontal components. For the ith event and jth site, we form the ratio $Sa_{ij}(P_k)/Sa_{ij}^{ref}(P_k)$, where $Sa_{ij}(P_k)$ is the absolute spectral acceleration (averaged over horizontal components) from SCEC-CVM event i at site j and period P_k, and $Sa_{ij}^{ref}(P_k)$ is the corresponding quantity for the corresponding reference-model event. Then we form the source-averaged basin response factor $B(D_q, P_k)$ by averaging over all N_{site} sites (N_{site}=1600), and over all N_{ev} events, where in this case N_{ev} is 10:

$$B(D_q, P_k) = \left(N_{ev} \sum_{j=1}^{N_{site}} W_{qj} \right)^{-1} \sum_{i=1}^{N_{ev}} \sum_{j=1}^{N_{site}} W_{qj} Sa_{ij}(P_k) / Sa_{ij}^{ref}(P_k)$$

Results

Figure 5, which shows *B* as a function of depth and period, summarizes the results of this procedure for (200 m bins). The main results from Fig 5 are the following: (1) Source-averaged basin amplification is period-dependent, with the highest amplifications occurring for the longest periods and greatest basin depths. (2) Relative to the very-hard rock reference structure, the maximum amplification is about a factor of 8. (3) Compared with 1D theoretical predictions, the 3D response is in most cases substantially higher. (4) The 3D response is also smoother, as a function of depth and period, than is the 1D prediction, since laterally propagating waves in the former smooth out the resonances present in the latter.
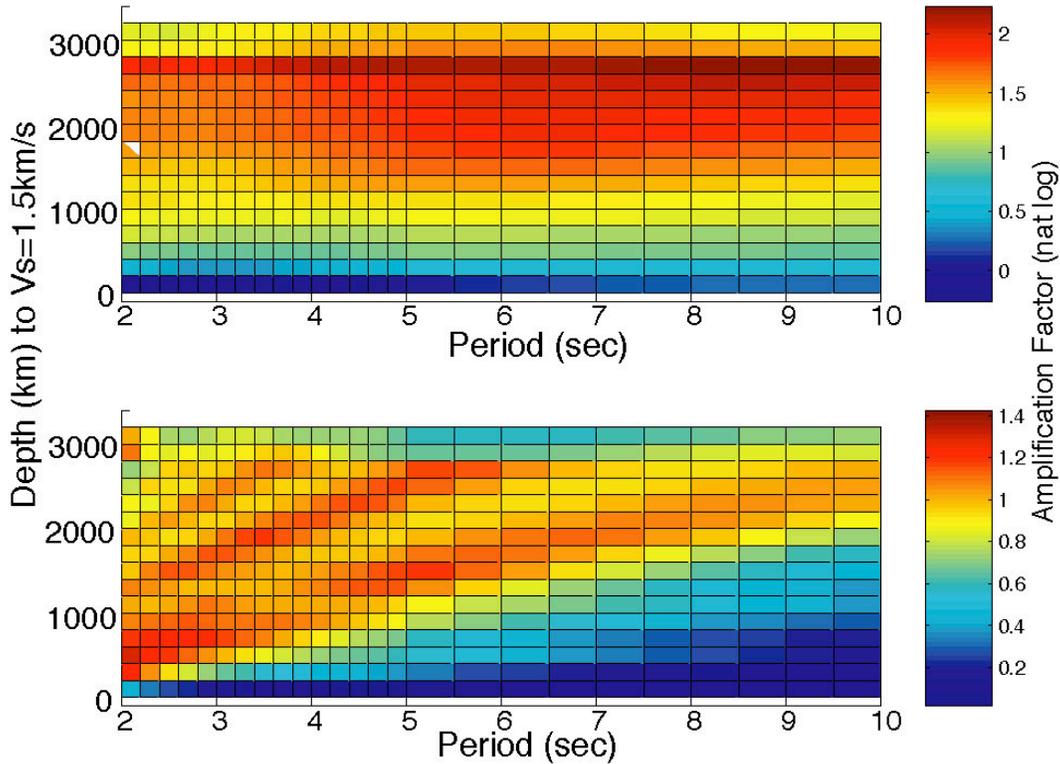
Figure 5. Top: Basin amplification versus depth and period, calculated from 3D simulations. Bottom: Basin amplification calculated by same procedure, but replacing the 3D results with 1D plane-wave amplification factors calculated using the local 1D wavespeed and density profiles (from the SCEC CVM) at each of the 1600 sites.

Figure 6 presents the results in the form of amplification curves for each of 6 periods. For depths in the range of roughly 500-1000 m, amplification decreases with period. This is, at least qualitatively, in agreement with expectations from 1D theory: shallow sediments will have diminished effect as the wavelength becomes long relative to sediment depth. For depths exceeding about 1000 m, amplification increases with period.

This is a 3D effect: higher-mode resonances present in the 1D case are smoothed out by lateral scattering, so that the longer-period resonances dominate.
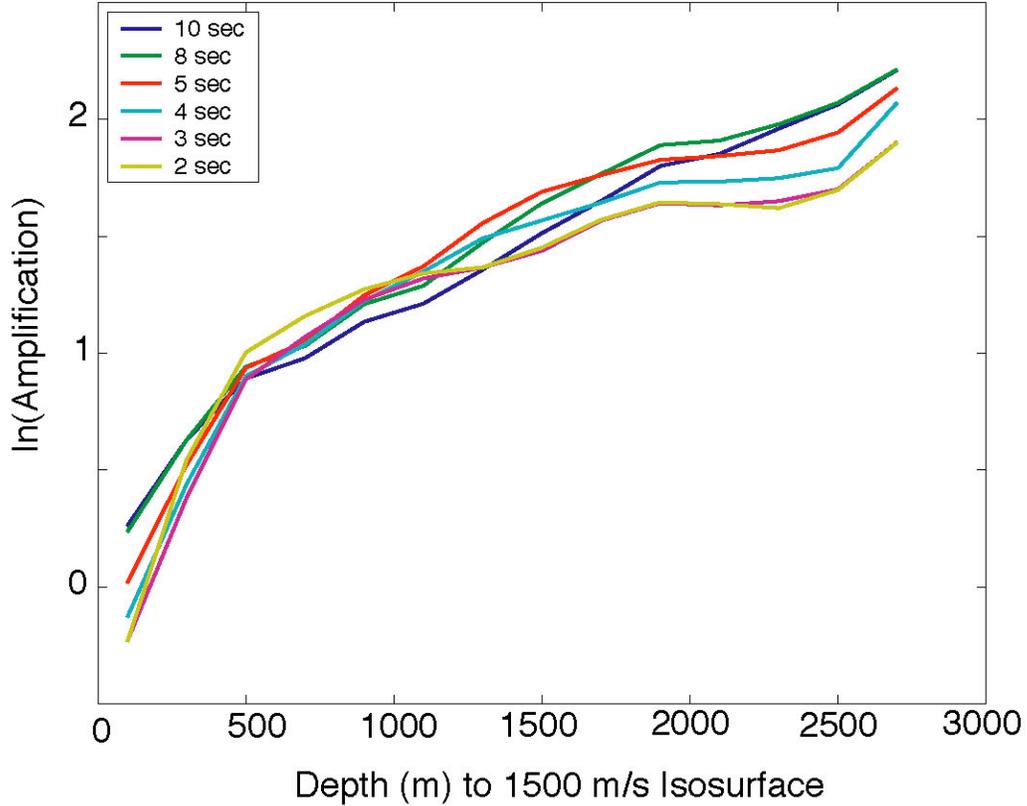
Figure 6. Basin amplification as a function of depth to 1.5 km/s S wave isosurface.

Parametric Model

It is useful to have a simple functional form that captures the main elements of the period- and depth-dependent basin amplification behavior observed in the simulations. One purpose of such a representation is to provide a functional form for representing basin effects in regression modeling of empirical ground motion data. We constructed a preliminary representation of this sort to provide immediate guidance to the NGA development team. Our approximate representation, $\tilde{B}(D,P)$ takes the following form:

$$\tilde{B}(D,P) = a_0(P) + a_1(P)\left[1 - \exp(D/300)\right] + a_2(P)\left[1 - \exp(D/4000)\right]$$

where

$$a_i(P) = b_i + c_i P, \ i=0,1,2 ,$$

14

The 6 parameters b_i, c_i were calculated in a two-step procedure. Separate least squares fits at each period P_k of $\tilde{B}(D,P_k)$ to $B(D_q,P_k)$ gave individual estimates of the $a_i(P_k)$ values for each period P_k. Then parameters b_i and c_i, for each i=0,1,2, were obtained by least-squares fitting of these 26 individual $a_i(P_k)$ estimates. The resulting values are

b_0=-1.06 c_0=0.124
b_1=2.26 c_1=-0.198
b_2=1.04 c_2=0.261

     The resulting amplification curves are shown in Fig 7. These expressions, despite their simplicity, represent the mean predictions of the numerical simulations quite well, and can serve as a starting point for modeling basin effects in empirical studies. In particular, they provide, in simple form, a physical basis for extrapolation of empirical models to periods greater than 2 or 3 seconds, where reliable data on basin effects are extremely scarce.
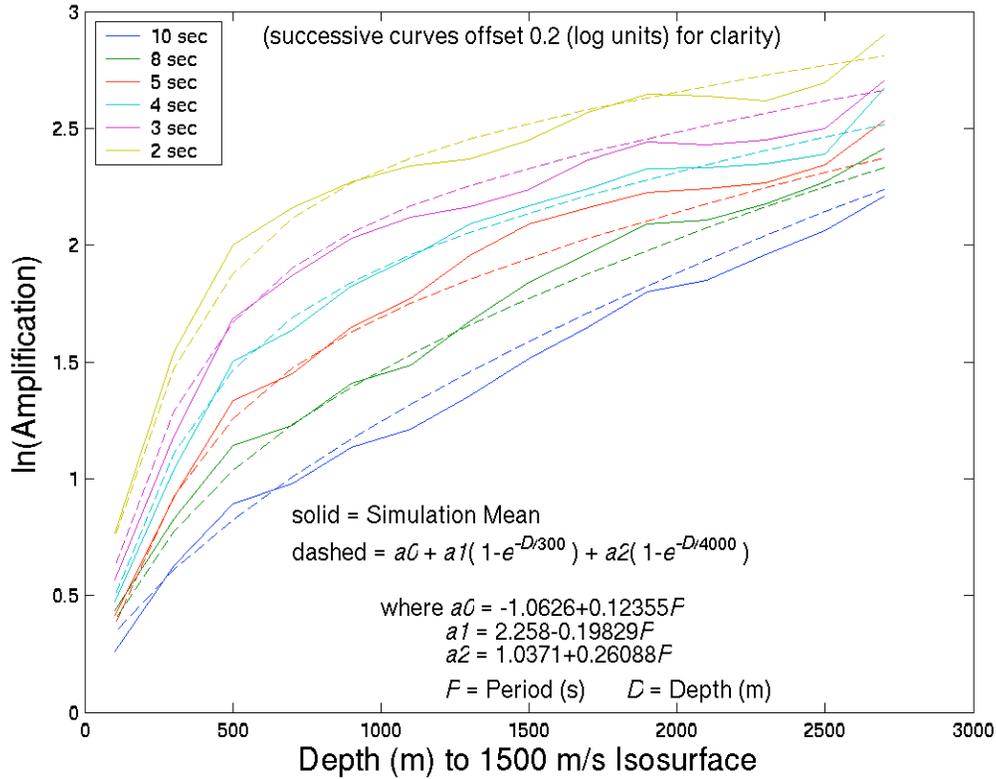
Figure 7. Parametric model $\tilde{B}$ (dashed curves) fit to basin amplification curves B (solid curves) derived by averaging 3D simulations.

Figure 8 shows the root mean square residual of $Sa_{ij}(P)\big/Sa_{ij}^{ref}(P)$, relative to $\tilde{B}(D,P)$, as a function of period. That is, the figure depicts R, where

15

$$\mathrm{R}^2\left(P_k\right) = \left(N_{ev}\sum_{j=1}^{N_{site}}W_{qj}\right)^{-1}\sum_{i=1}^{N_{ev}}\sum_{j=1}^{N_{site}}\left[Sa_{ij}(P_k)\Big/Sa_{ij}^{ref}(P_k) - \tilde{B}\left(D_j,P_k\right)\right]^2.$$

The residuals decrease systematically with period. This period-dependence is what one would expect on the basis of simple physical arguments. Short-period waves are subject to short-wavelength variations due to local focusing and interference effects. Very long-period waves, in contrast, represent oscillations that are coherent over large scale lengths and are influenced principally by large-scale averages of the seismic velocity structure.
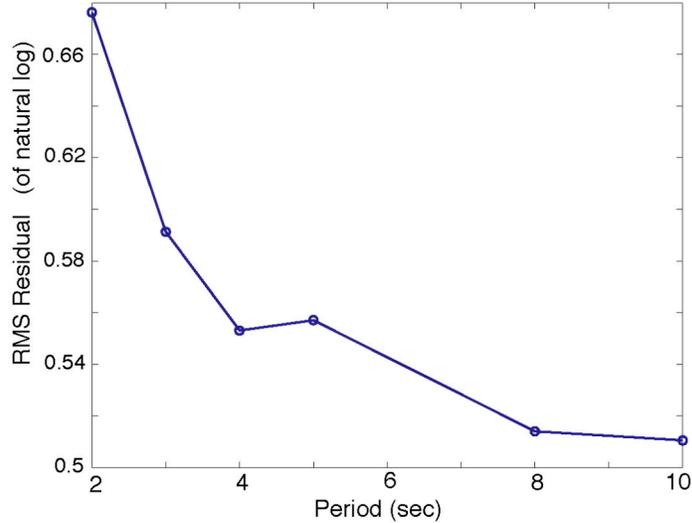
Figure 8. Root-mean-square residual of spectral acceleration amplification, relative to predictions from parametric model.

CONNECTION TO ATTENUATION RELATIONS

The parametric relationships developed in the last section are preliminary, and designed to guide the design of functional forms for use in attenuation relationships for elastic response spectra. In particular, they should be useful guides for extrapolating the period-dependence to periods longer than a few seconds, where empirical data provide little constraint.

On the other hand, we caution that these preliminary parametric relationships should not be used quantitatively to correct attenuation relationships for the basin depth effect. Such direct, quantitative use of the results may become possible in the future, however. The main requirement is that we first carefully assess the extent to which the basin effect, as defined and quantified in this study, is already accounted for implicitly in existing attenuation relationships, through (1) departures of the average "rock" site from our idealized reference model, and (2) correlation of basin depth with other predictor variables (such as Vs_{30}).

As a very rough assessment of the difference between our hard-rock reference model and the average real "rock" site, we compare long-period (5 s) spectral amplitudes from the reference simulations with a standard empirical rock regression relationship.

Five seconds is sufficiently long period that the details of the source will have minimal importance, and the main source of bias between the mean theoretical and empirical predictions is likely to be the difference between our idealized high-velocity reference model and the typical rock-site velocity structure (principally at shallow depth, roughly the uppermost several hundred meters). We find that the reference-model simulations under-predict the rock regression model of Abrahamson and Silva (1997) by a factor of 2. Hence, as a first approximation, the basin-depth factors can be scaled down by a factor of 2 to convert them to correction factors to empirical rock-site relationships. For D=2.5 km example, the resulting correction to rock-site relationships is about 2.75 at 2 s period, and 3.75 at 10 s period. The correction factors are lower for shallower basin sites, and the period dependence has the reverse sense. For example, for D=0.75 km, the corresponding factors are approximately 1.7 (at 2 s) and 1.4 (10 s).

The factor of 2 long-period bias between hard-rock simulations and empirical rock-site regression models suggests that the standard rock-site classification actually incorporates sites in which relatively low S velocities (less than ~2 km/s) extend, on average, to depths of the order of 0.5 km. Our preliminary recommendation, therefore, is that the basin response functions be used as a guide to the functional form of the depth and period dependence of the basin effect for depths (to the 1.5 km/s isosurface) greater than about 400-500 m, as suggested by Fig 9.
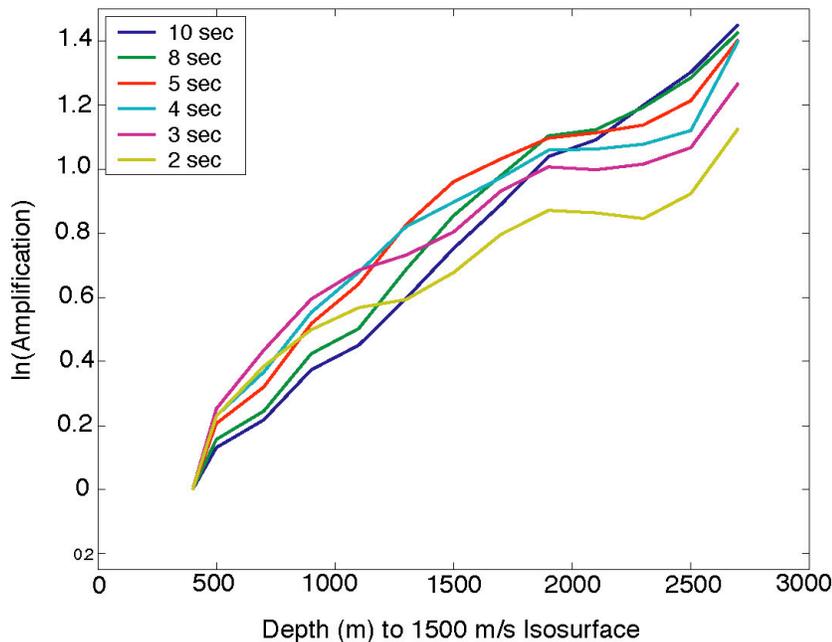
Figure 9. Basin response functions restricted to (1.5 km/s isosurface) depths exceeding 400 m.

REFERENCES

Abrahamson, N. A., and W. J. Silva (1997). Empirical response spectral attenuation relations for shallow crustal earthquakes, *Seism. Res. Lett.* 68, 94-127.

Day, S. M., J. Bielak, D. Dreger, R. Graves, S. Larsen, K. Olsen, and A. Pitarka (2003). Tests of 3D elastodynamic codes: Final report for Lifelines Project 1A02, Pacific Earthquake Engineering Research Center.

Day, S. M., J. Bielak, D. Dreger, R. Graves, S. Larsen, K. Olsen, and A. Pitarka (2003). Tests of 3D elastodynamic codes: Final report for Lifelines Project 1A01, Pacific Earthquake Engineering Research Center.

Magistrale, H., S. M. Day, R. Clayton, and R.W. Graves (2000). The SCEC southern California reference three-dimensional seismic velocity model version 2,.*Bull. Seism. Soc. Am., 90*, S65-S76.

Olsen, K. B., S. M. Day, and C. R. Bradley (2003). Estimation of Q for long-period (>2 s) waves in the Los Angeles Basin, *Bull Seism. Soc. Am*, *Vol 93*, 627-638.

Somerville, P.G., K. Irikura, R, Graves, S. Sawada, D. Wald, N. Abrahamson, Y. Iwasaki, T. Kagawa, N. Smith and A. Kowada (1999). Characterizing crustal earthquake slip models for the prediction of strong ground motion. *Seism. Res. Lett. 70,* 59-80.